Ex-situ nitrogen-doped porous carbons as electrode materials for high performance supercapacitor

Ndeye F. Sylla [a], Ndeye M. Ndiaye [a], Balla D. Ngom [b], Bridget K. Mutuma [a], Damilola Momodu [a], Mohamed Chaker [c], and Ncholu Manyala [a]*

[a] Department of Physics, Institute of Applied Materials, SARChI Chair in Carbon Technology and Materials, University of Pretoria, Pretoria 0028, South Africa

[b] Laboratoire de Photonique Quantique, d'Energie et de Nano-Fabrication, Faculté des Sciences et Techniques Université Cheikh Anta Diop de Dakar (UCAD) B.P. 5005 Dakar-Fann Dakar, Sénégal

[c] Institut National de la Recherche Scientifique Centre – Énergie Matériaux Télécommunications 1650, Boul. Lionel Boulet, Varennes (Québec) J3X 1S2 Canada

*Corresponding author email: ncholu.manyala@up.ac.za, Tel: + (27)12 420 3549

Fax: + (27)12 420 2516

Abstract

Nitrogen (N) doping of porous carbon materials is an effective strategy for enhancing the electrochemical performance of electrode materials. Herein, we report on *ex-situ* (*post*) nitrogen-doped porous carbons prepared using a biomass waste, peanut shell (PS) as a carbon source and melamine as the nitrogen source. The synthesis method involved a two-step mechanism, initial chemical activation of the PS using KOH and *post* N-doping of the activated carbon. The effect of the activating agent/precursor ratio and the *ex-situ* N-doping on the structural, textural, electrochemical properties of the porous carbons was studied. The *ex-situ* N-doped porous carbon with an optimum amount of KOH to PS exhibited the best capacitance performance with a specific surface area (SSA) of 1442 m^2 g^{-1} and an enriched nitrogen content (3.2 at %). The fabricated symmetric device exhibited a 251.2 F g^{-1} specific capacitance per electrode at a gravimetric current of 1 A g^{-1} in aqueous electrolyte (2.5 M KNO_3) at a wide cell voltage of 2.0 V. A specific energy of 35 Wh kg^{-1} with a corresponding specific power of 1 kW kg^{-1} at 1 A g^{-1} was delivered with the device still retaining up to 22 Wh kg^{-1} and a 20 kW kg^{-1} specific power even at 20 A g^{-1}. Moreover, long term device stability was exhibited with an 83.2% capacity retention over 20 000 charge/discharge cycles and also a good rate capability after 180 h of floating at 5 A g^{-1}. This great performance of the symmetric supercapacitor can be correlated to the surface porosity and *post* nitrogen-doping effect which increased the electrochemically-active sites resulting in a remarkable charge storage capability.

Keywords: Nitrogen-*doped carbon, biomass, porosity, chemical activation, supercapacitor*

Graphical Abstract

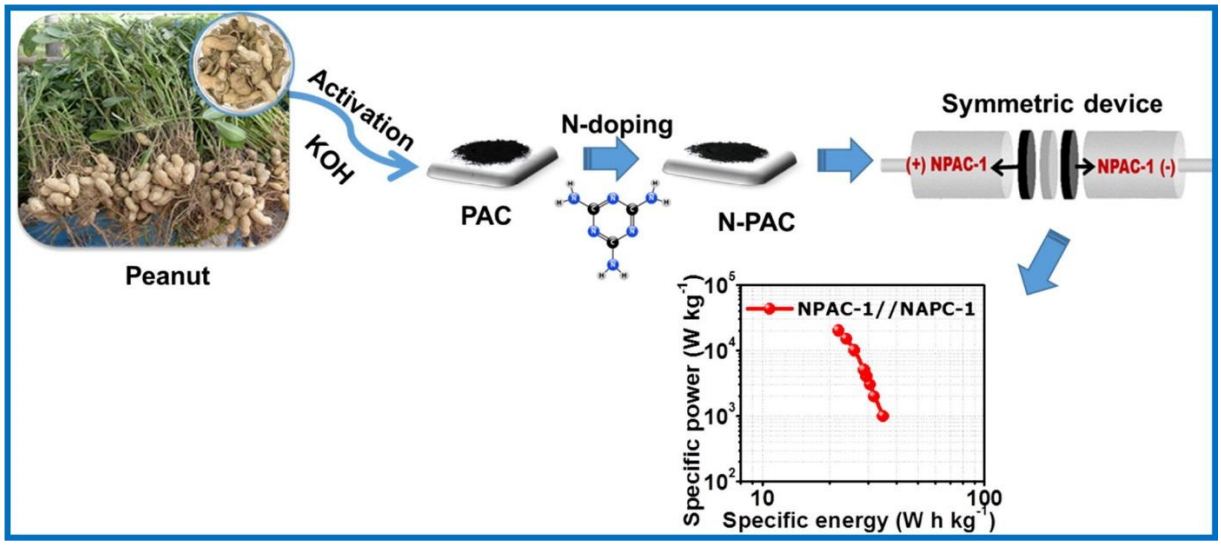

1. Introduction

Porous carbons have received considerable attention in the scientific community over recent years. They have been applied in various energy-related systems such as sensors, hydrogen storage, supercapacitors and batteries [1]. This is due to their high electrical conductivity, chemical and thermal stability, ease of processability and ability to tune their textural surface properties [2,3]. More importantly, these properties are advantageous in the fabrication of electrode materials for electrical double-layer capacitors (EDLCs). In principle, EDLCs energy storage mechanism entails an electrostatic interaction between the electrode/electrolyte interface. Therefore, the performance of the EDLCs depends on the reversible ion adsorption in the porous carbon electrode materials [4,5]. As such, the development of suitable porous materials with improved electrochemical performance has received immense efforts. These porous carbons can be derived from biomass [6,7], polymers [8,9], metal-organic frameworks [10,11] and zeolites [12,13], using a wide range of synthesis techniques such as physical and chemical activation [14], templating method [15], template-free method [16] and microwave irradiation [17] among others. During the synthesis of porous carbons, it is possible to tune

their physicochemical properties and surface features and consequently impact on their electrochemical performance.

Typically, the electrochemical performance of porous carbons is dependent on the surface area, electrical conductivity and the surface interaction between the electrode and the electrolyte interface [1]. Thus, several strategies have been developed to enhance the electrochemical performance of porous carbon-based electrode materials. One of the approaches involves the modification of the carbon surface chemistry by use of surface functionalization process [18–20]. For instance, Wu *et al.* [20] synthesized porous carbons using rod-like hydroxyapatite (as a template) and sucrose (carbon source) followed by an oxidation process using nitric acid (HNO_3).

The authors suggested that the modification of the surface chemistry of the porous carbons contributed to the improvement of the specific capacitance from 110 F g^{-1} in the non-modified carbons to 128 F g^{-1} in the modified counterparts. They correlated it to the increase in the oxygen content and the creation of new functional groups after acid treatment [20]. The surface functional groups play an important role in the enhancement of the surface wettability at the electrode/electrolyte interface and consequently improve the electrochemical performance of the electrode materials.

A second approach for improving the electrochemical performance of porous carbons is the two-step activation process that allows for the creation of a porous carbon network [21–23]. For example, Cheng *et al.* [21] used a two-step activation process to synthesize a porous activated carbon with hierarchical pore network and improved surface features. The first step involved the activation of shiitake mushroom with H_3PO_4 at 500 ^{0}C which exhibited a specific surface area (SSA) of 1341 m^2g^{-1} and a capacitance of 196 F g^{-1}. The second step was done by further activation of the carbon with KOH at 800 ^{0}C which yielded an improvement of SSA

and specific capacitance of 2988 m^2g^{-1} and 306 F g^{-1}, respectively. The two-step process aided in increasing the number of oxygenated functional groups on the carbon surface as well as the surface area as compared to the one-step activation.

Lastly, heteroatom doping of porous carbons with nitrogen (N), boron (B), oxygen (O), sulfur (S), and phosphorous (P) atoms has proved to enhance the electrochemical performance in supercapacitors [24–27]. It is well known that the incorporation of heteroatoms in the carbon matrix changes the electron-donating or accepting character and conductivity of carbons and thus, influencing their capacitance and electrochemical properties [28]. Compared to other heteroatoms, nitrogen is of great interest as its atomic size is comparable to that of carbon (65pm vs 70pm).

Therefore, different nitrogen-containing precursors such as melamine, urea, ammonia, polyaniline and polypyrrole have been used to synthesis N-doped porous carbons [29–32]. Two main approaches are employed for nitrogen doping of carbons; *in-situ* and *ex-situ* doping process [33]. *In-situ* doping treatment can be done either by direct pyrolysis of nitrogen-containing precursors for example organics polymers [34], biomass [35], ionic liquids [36] or by the growth of carbon nanomaterials in the presence of a nitrogen precursor [37]. In this regard, *in-situ* nitrogen-doping of activated carbons can be carried out by direct activation of nitrogen-containing biomass or by the activation of carbonaceous sources in the presence of a nitrogen-containing precursor. The main drawback of this process is that most of the oxygenated nitrogen groups are lost at higher temperatures (during activation) resulting in a lower nitrogen content being incorporated within the carbon matrix.

In our previous work, we synthesized an *in situ* N-doped porous carbon by the direct pyrolysis of a mixture of peanut shell waste biomass (carbon source) and urea (as a nitrogen source) at 600 °C followed by activation at high temperature (850 °C) [38]. We obtained a low nitrogen

(0.6 at%) content and this was attributed to the volatilization of the nitrogen-containing groups during the activation step. To circumvent this problem, we propose the *ex-situ* N-doping of porous carbons as it will allow the incorporation of larger nitrogen content within the carbon matrix. Typically, the *ex-situ* N-doping process requires the introduction of nitrogen source into the matrix of an already activated porous carbon nanomaterial via thermal treatment [39]. While the amount of nitrogen content incorporated in porous carbons can be controlled by the precursor used, ammonia gas is the commonly used source of nitrogen which not only limits the N-content but is also not environmental friendly [40]. Moreover, most of the studies on N-doped porous carbons emphasize the effect of the mass ratio of carbon to nitrogen (C/N) precursor as well as the doping temperature effects [39,41]. To this end, very few reports exist on the effects of the mass ratio of activating agents on *ex-situ* N-doped activated carbons and their application in supercapacitors.

In the present study, the properties of the *ex-situ* nitrogen-doped porous carbons obtained from peanut shell are investigated. The synthesis method involved two steps mechanism: (1) Chemical activation of the peanut shell using KOH, and (2) nitrogen doping of the porous peanut activated carbon. Their electrochemical performances were evaluated in a three and two-electrode configuration using an aqueous electrolyte (2.5 M KNO_3). The effect of the activating agent/precursor ratio (KOH/PS) and the *ex-situ* N-doping on the electrochemical behaviour was studied. Despite the many reports on biomass-derived porous carbon materials in the literature, to the best of our knowledge, studies on the strong influence of the chemical activation ratio and *ex-situ* N-doping on the electrochemical performance of these materials have been rarely reported. Thus, this study will not only provide a procedure for retaining the relatively high N-doping concentration but also elucidate the vital role of textural and structural parameters for optimum electrochemical properties of N-doped porous carbons in supercapacitors.

2. Experimental section

2.1 Precursor materials

The peanut shell waste used in this study was collected from a marketplace in downtown Saint Louis, Senegal. Argon gas, Ar (99%) was purchased from Afrox, South Africa. Potassium hydroxide, KOH (99 %), melamine,$C_3H_6N_6$ (99%), hydrochloric acid, HCl (37%), potassium nitrate, KNO_3 (99.99%), carbon acetylene black (99.95%), polyvinylidene fluoride, PVDF (99%) and N-methyl-2-pyrrolidone, NMP (99%), were all purchased from Merck (Pty) Ltd, South Africa. Polycrystalline nickel foam with an areal density of 420 g m^{-2} and 1.6 mm thickness and microfiber filter paper (0.18 mm thickness) were procured from Alantum Munich, Germany, and ACE chemicals, South Africa, respectively.

2.2 Preparation of pristine and *ex-situ* N-doped activated carbons

The peanut shell (PS) waste serving as a raw material (RM) was thoroughly washed with deionized water (DI) and dried in an oven pre-set at 60 °C. The RM was ground and mixed with potassium hydroxide activating agent (AA) in different mass ratios of 1:0.5, 1:1 and 1:2 (PS:AA). The mixture was transferred into a tubular furnace and heated-up to 850 °C at a heating rate of 5 °C min^{-1} under argon gas and held at the final temperature for 1 h. The obtained product was impregnated with aqueous 3 M HCl to remove all traces of unreacted AA, sonicated for 12 h and then washed with DI until a neutral pH was achieved. Thereafter, the solid peanut shell activated carbon sample was filtered and labelled as PAC-0.5, PAC-1 and PAC-2 for PS:AA mass ratios of 1:0.5, 1:1 and 1:2, respectively. These samples were dried for further characterization.

An *ex-situ-doping* route was used to prepare the nitrogen-doped peanut shell activated carbon (NPAC). Firstly, 5 g of melamine used as a nitrogen source was added to 1 g of the as-

synthesized PAC-0.5 sample in an optimized mass ratio. Pyrolysis of the sample at 850 °C was carried out for 1 h under a stream of inert argon gas to produce NPAC-0.5. A similar *ex-situ-doping* procedure was undertaken for the PAC-1 and PAC-2 samples to yield NPAC-1 and NPAC-2, respectively. To further emphasize this unique *ex-situ-doping* concept applied in this study, melamine was introduced prior to activation for a good comparison. The nitrogen content in NPAC-samples was compared from characterization carried out.

2.3 Material characterization

The N_2 sorption isotherms of the samples were measured at 77 K from 0.01 to 1.0 relative pressure (P/P_o) using a Micrometrics TriStar II 3020 pore analyzer. The active surface area was determined using the Brunauer-Emmett-Teller (BET) method and the Barrett-Joyner-Halenda (BJH) method was used to describe the pore size distribution. A 532 nm laser-powered WITec alpha300 RAS+ confocal Raman microscope (WITec, Germany) was used for the detailed Raman analysis. A PANalaytical X'Pert Pro powder diffractometer with Co-Kα radiation (λ=1.789Å) was used to collate the X-ray diffraction (XRD) patterns. The surface morphology of the PAC and NPAC samples were characterized on a Zeiss Ultra-plus 55 field emission scanning electron microscope (FE-SEM) operated at 1.0 kV. The chemical composition of the NPAC samples was analyzed by X-ray photoelectron spectroscopy (XPS, VG Escalab 220i-XL) coupled with a monochromatic aluminium Kα source of radiation.

2.4 Electrochemical characterization

The working electrodes used for electrochemical analysis were fabricated with 80 wt% active materials, 10 wt% carbon acetylene black and 10 wt% polyvinylidene difluoride (PVDF) in an agate mortar with the final addition of few drops of N-methylpyrrolidone (NMP) to form a

slurry. The slurry was coated on clean Nickel foam (NF) grids followed by subsequent vacuum drying of the electrodes for 12 h at 80 °C.

The electrode materials' electrochemical performances in half- and full-cell configurations were evaluated in 2.5 M KNO_3 aqueous electrolyte using a Bio-Logic VMP-300 16-channel potentiostat (Knoxville, USA) at room temperature. The three-electrode (half-cell) measurements were performed using a Swagelok T-cell composed of silver (Ag)-disc reference electrode, carbon disc counter electrode and a microfiber filter paper separator.

The symmetric devices were assembled in the Swagelok testing cell using similar materials present on both electrodes with the charge/mass balancing taken into consideration. The cyclic voltammetry (CV) profiles were evaluated at different scan rates (in mV s^{-1}) and the galvanostatic charge-discharge (GCD) plots were obtained by varying the specific current (in A g^{-1}). The electrochemical impedance spectroscopy (EIS) measurements were done on an open circuit voltage, V_{OC} at 100 kHz to 10 mHz frequency range.

The specific capacitance for the half cell C_s (in F g^{-1}) and the single electrode for the symmetric device C_{el} (in F g^{-1}) was determined from the discharge slope of the GCD plots using the Eqs. (1) and (2), respectively [42,43]:

$$C_s = \frac{I\Delta t}{m\Delta V} \quad (1)$$

$$C_{el} = 4\frac{I\Delta t}{m\Delta V} \quad (2)$$

where I (in A) is the current, m (in g) represent the total mass of the electrode Δt (in seconds) is the discharge time from the slop of GCD, and ΔV (in V) is the operating voltage.

The specific energy E_d (Wh kg^{-1}) and the specific power P_d (W kg^{-1}) for the symmetric device were evaluated according to the Eqs. (3) and (4) [44]:

$$E_d = \frac{C_{el}(\Delta V)^2}{28.8} \quad (3)$$

$$P_d = 3600\frac{E_d}{\Delta t} \quad (4)$$

3. Results and discussion

3.1. Morphological, Textural and Structural characterization

Fig. 1 shows the SEM images of the pristine and the N-doped PAC samples at low and high magnification (see insets to images). All the synthesized carbon materials displayed an interconnected porous structure with irregular-shaped pores. It can be seen that the activation of the peanut shell with potassium hydroxide leads to the creation of a porous framework on the structure of the carbons. This is expected to occur due to the release of carbon monoxide (CO) and carbon dioxide (CO_2) gases upon the reaction of KOH and carbon [45]. The decomposition of the KOH generates potassium bicarbonate, metallic potassium and hydrogen gas. At elevated temperatures (>700 ^{0}C) the decomposition of the potassium bicarbonate produces CO_2 and CO gases which promotes further pore activation through carbon gasification [46,47]. The as-prepared PACs display a tunable morphology and porous structure as shown in Fig. 1(a), (c) and (e).

In addition, the increase of the mass ratio of KOH from 0.5 to 1 resulted in a more evident porous morphology (PAC-1 in Fig. 1(c)). However, upon a mass ratio increase of KOH to 2, a highly distorted interconnected porous structure in the PAC-2 was observed (Fig. 1(e)). After nitrogen doping, the morphology of the NPACs materials exhibited a less porous structure as compared to their pristine counterparts (Fig. 1(b), (d) and (f)). This could be ascribed to the carbon and nitrogen (C/N) patches emanating from melamine decomposition that can block the already existing pores on the carbon matrix during the *ex-situ* nitrogen doping step [18] [48].

The electron dispersive spectroscopy (EDS) elemental mapping was carried out to determine the elemental composition of the N-PAC samples with an example of N-PAC-1 shown in Fig. S1. This EDS mapping reveals a uniform distribution of the C, O and N elements which similar to all N-PAC samples.

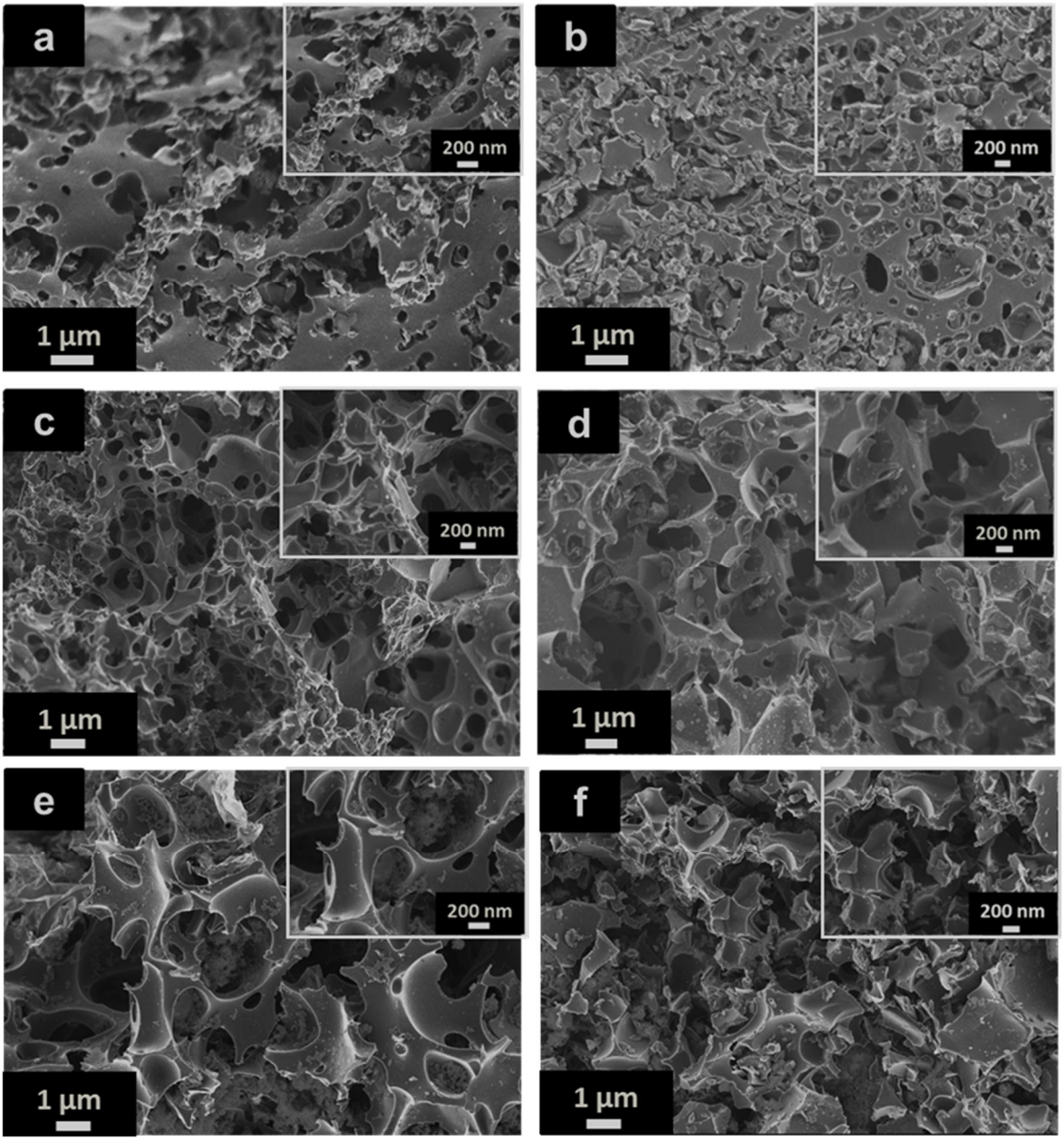

Fig. 1. SEM images of the pristine (a) PAC-0.5, (c) PAC-1, (e) PAC-2 and N-doped (b) NAP-0.5, (d) NPAC-1 and (f) NPAC-2 samples at low magnification (insets showing the high magnification).

The textural properties of the PAC and NPAC samples were investigated by nitrogen sorption isotherms and the pore size distribution analysis. Fig. 2(a-b) revealed the N_2 adsorption-desorption isotherms of the PACs and NPACs samples with different mass ratios of (PS:AA) 1:0.5, 1:1 and 1:2.

The isotherm curves of all the samples showed a hybrid type I and IV characteristics with a H4 hysteresis loop suggesting the presence of micropores and mesopores [49]. At a low relative pressure range, the isotherms of the obtained PACs and NPACs showed steep N_2 adsorption exhibiting an abundant presence of micropores besides the hysteresis loop reflecting the presence of mesopores. The pore size distribution plots illustrated in Fig. 2(c-d) confirm the existence of both the micropores and mesopores in the pristine (undoped) and N-doped carbon derived from peanut shell.

Table 1. summarizes the textural properties of the PAC and NPAC samples. It is evident that the BET specific surface area (SSA) increases with increasing mass ratio of KOH from 0.5 to 1 and decreases with a further increase to 2. A similar trend is noticed for the total pore volume and the micropore volume of the carbon materials. The PAC-1 and NPAC-1 samples exhibit the highest surface areas of 1557 $m^2 g^{-1}$ and 1442 $m^2 g^{-1}$ as well as the highest pore volumes of 0.76 $cm^3 g^{-1}$ and 0.69 $cm^3 g^{-1}$, respectively. These results demonstrate the creation of stable pores that contribute to the SSA improvement with activation using a moderate KOH content. However, the lowest SSA assigned to the PAC-2 and NPAC-2 materials (548 $m^2 g^{-1}$ and 437 $m^2 g^{-1}$) could be attributed to the excess amount of KOH as well as less extent of activation as further affirmed by the decrease in the total pore volume and the micropore volume as depicted in Table 1. The excessive amount of KOH may have resulted in saturation of the reaction sites with unreacted KOH that inhibited the creation of extra pores after a particular point during the process of pores creation. This leads to the inhibition of pore creation and also the collapse of the interconnected carbon [50]. The SSA of the NPAC-1 and NPAC-2 materials was found to

be slightly lower than that of the PAC-1 and PAC-2. As proposed earlier from the morphology results, this can be ascribed to the decomposition of melamine into patches of nitrogen-containing functionalities (carbon/nitrogen deposits) which can cover some of the pre-existing pores in the PAC [19].

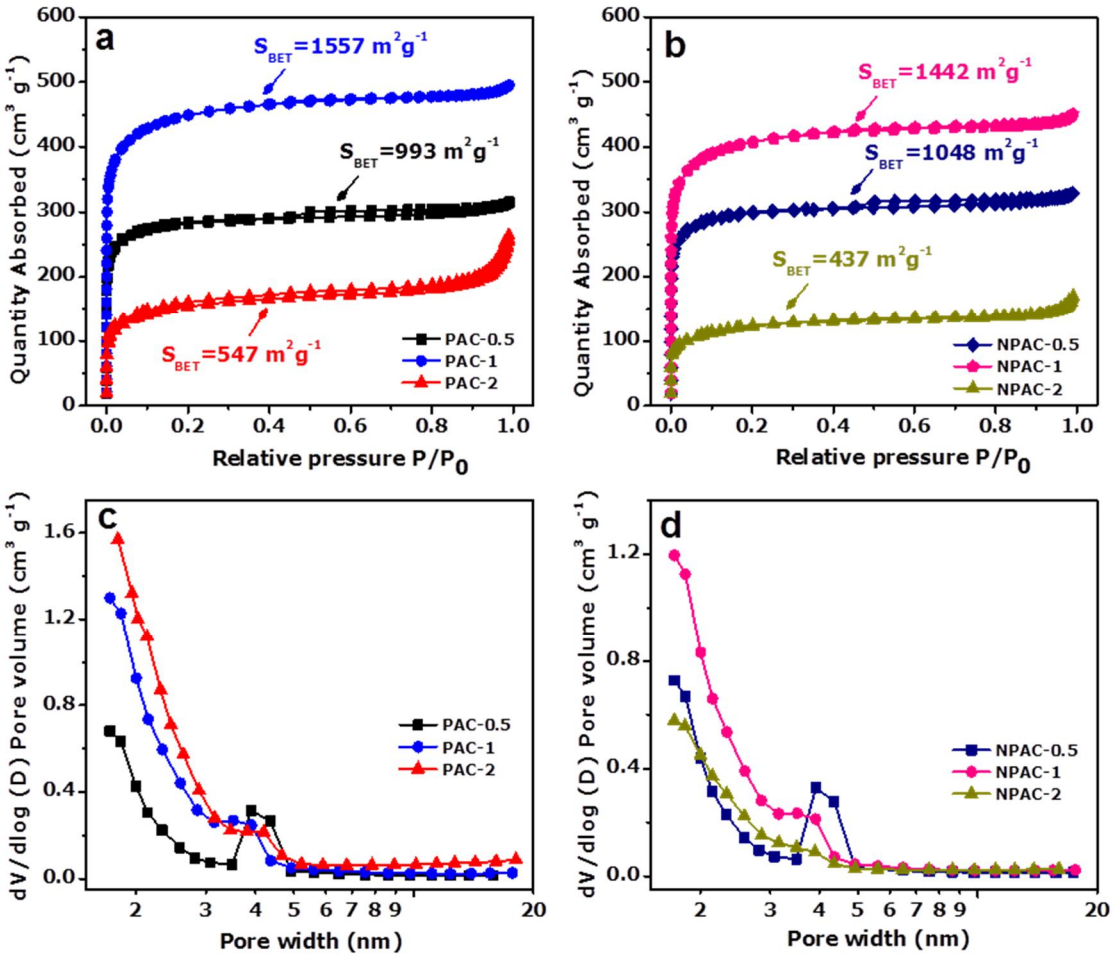

Fig. 2. (a-b) N_2 absorption-desorption isotherms; (c-d) pore size distribution of the pristine and N-doped samples obtained at different mass ratios of KOH.

In addition, the ex-situ N-doping of the carbons with melamine can cause the destruction of the pore walls and the blockage of some of the pores by the functional groups [18]. Consequently, NPAC-1 and NPAC-2 displayed lower pore volumes as compared to PAC-1 and PAC-2, respectively. This decrease in surface area and pore volume upon *ex-situ* N-doping of PAC

materials has been observed elsewhere and is in agreement with those studies on N-doped carbons [48,51,52].

Table 1. Textural properties and Raman data of the pristine and N-doped samples

Samples		Textural properties			Raman data		
		S_{BET} (m^2 g^{-1})	V_{total} (cm^3 g^{-1})	V_{micro} (cm^3 g^{-1})	D-band (cm^{-1})	G-band (cm^{-1})	I_D/I_G ratio
Pristine	PAC-0.5	993	0.48	0.42	1339	1589	0.95
	PAC-1	1557	0.76	0.63	1341	1590	0.96
	PAC-2	548	0.38	0.19	1348	1591	0.98
N-doped	NPAC-0.5	1048	0.50	0.43	1342	1590	1.02
	NPAC-1	1442	0.69	0.59	1340	1591	1.03
	NPAC-2	437	0.25	0.15	1344	1590	1.21

The structure of the as-prepared carbon samples was further investigated by Raman spectroscopy and XRD. Fig. 3(a-b) display the Raman spectra of the pristine and the N-doped carbon materials at different mass ratios of potassium hydroxide. The spectra of all samples show the D peak (1339-1348 cm^{-1}) and G peak (1589-1591 cm^{-1}) bands attributed to the disorder (defect) in the graphitic structure and the tangential vibration of the sp^2 carbon atoms, respectively [53]. The ratio of the relative intensity of the D and G peaks (I_D/I_G) is used to determine the graphitization degree of the carbon materials [54]. The I_D/I_G values of PACs and NPACs (as shown in table 1) indicate that increasing the mass ratio of the KOH led to a higher degree of disorder (higher I_D/I_G ratios) in the carbon matrix. These results suggest that the KOH activation could generate more active sites in the carbon structure corresponding to other previous reports on activated carbons [55,56]. Fascinatingly, the NPAC samples revealed even higher I_D/I_G values as compared to the pristine carbons (PAC). This can be ascribed to the introduction of nitrogen in the carbon structure creating more structural distortions which affect the intensity of the D band [57]. The presence of even more defective sites on the graphitic lattice could aid electrochemical surface reactions.

Fig. 3(c-d) show the XRD patterns of the as-prepared carbon samples. The PACs and NPACs samples display two diffraction peaks at 2θ values of 26˚ and 51˚ which correspond to the (002) and (012) planes in the graphite structure, respectively. These peaks were broad indicating that all the carbon materials are amorphous carbon confirming the low degree of graphitic crystalline structure [58]. However, the diffraction peaks of N-doped carbon samples are slightly shifted to higher 2 theta values compared those of undoped samples, which are due to the incorporation of nitrogen in the carbon [59].

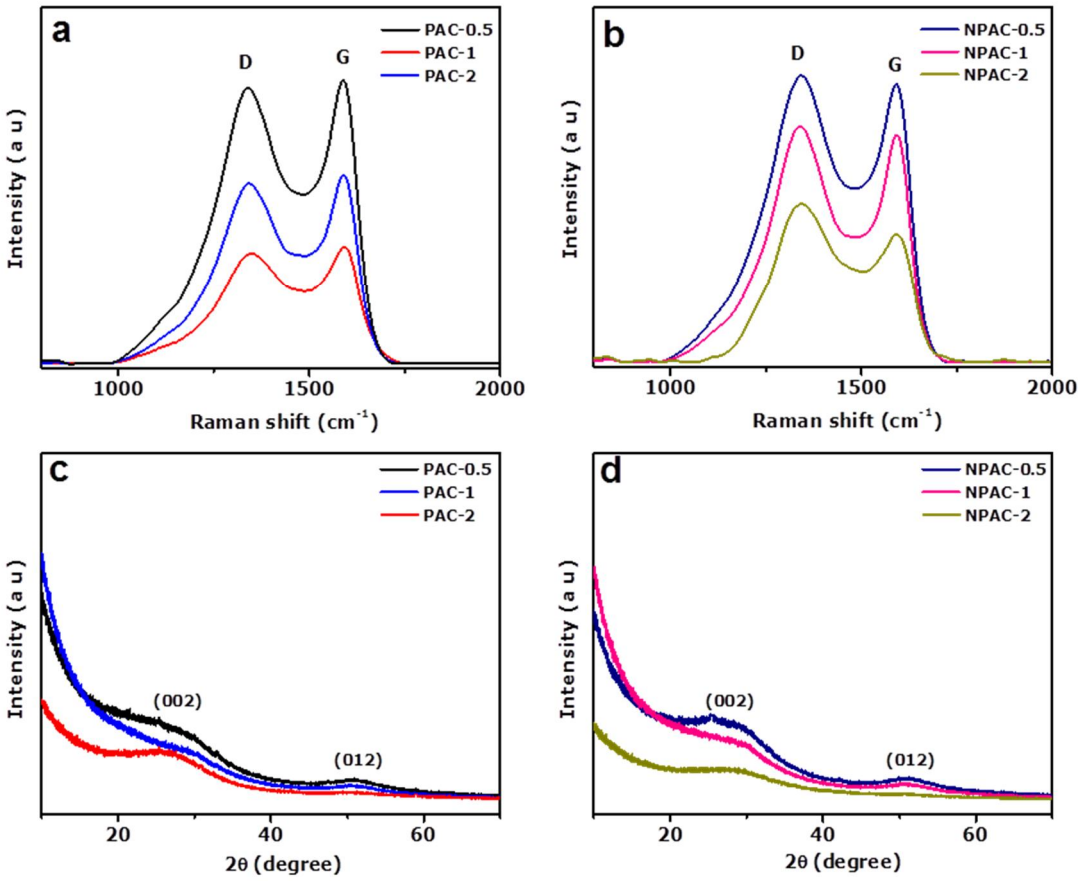

Fig. 3. (a-b) Raman spectra and (c-d) XRD pattern of the pristine and the N-doped samples.

3.2 ***XPS analysis***

The XPS analysis was performed to determine the chemical composition and surface chemistry after the N-doping process of the pristine activated carbon materials. Fig. 4(a) displays the XPS survey spectra of the NPAC-0.5, NPAC-1 and NPAC-2 samples which indicated the presence of three peaks C1s (285 eV), N1s (399 eV) and O1s (533 eV) confirming the successful

incorporation of the nitrogen atoms into the carbon matrix. The atomic percentages (% at) of each component calculated from the integral peak area of the XPS data is shown in Table 2. It can be seen that as the KOH activation mass ratio increases, the nitrogen content decreases from 6.4 at.% for NPAC-0.5 to 3.2 at.% for the NPAC-1 then increases to 8.9 wt.% for the NPAC-2.

Table 2. Elemental composition of the NPAC materials

Samples	Elemental Composition (at.%)		
	C	O	N
NPAC-0.5	87.9	5.8	6.3
NPAC-1	94.0	2.8	3.2
NPAC-2	80.5	10.6	8.9

The NPAC-1 showed the lowest N and O content owing to the creation of more pores on the surface at the optimum activation ratio. NPAC-1 displayed the highest carbon content and the lowest oxygen content suggesting that most of the nitrogen atoms were attached to the carbon atoms in the form of pyrrolic-N, pyridinic-N and graphitic-N. The lowest oxygen content in NPAC-1 is associated with the initial oxygen content in the undoped PAC-1 as recorded in the supporting information (Table S1.). Similarly, the high N content for NPAC-2 could be ascribed to the formation of carbon and nitrogen deposit over the collapsed carbon structure thus increasing the amount of nitrogen and oxygen functionalities [18]. This is in agreement with the lower surface area and pore volume values reported for the NPAC material. Moreover, the high N and O content in NPAC-2 sample confirms the presence of a high number of structural defects (high I_D/I_G) as observed from the Raman data.

The different chemical environments of the carbon, nitrogen and oxygen atoms in the NPAC samples were determined by deconvolution of the high-resolution XPS spectra of the C1s, N1s and O1s peaks (Figs. 4(b-d) and S2). In addition, the XPS data of the undoped PAC-1 sample is given in the supplementary information (Fig. S4) as an example of all the PAC samples. It

is clear that for the pristine PAC samples, there is no nitrogen which confirms the presence of the nitrogen in N-PAC samples is due to the melamine. The high resolution of the core level C1s spectra (Fig. S2(a-c)) were deconvoluted into three component peaks. The main peak 284.4 eV is ascribed to the sp^2 hybridized carbon (C=C), while the two other peaks at 285.5 eV and 287.0 eV are associated to the sp^3 hybridized carbon (C-C) or C-N and O–C=O, respectively [60,61]. Fig. 4(b-d) reveals the high resolution of the N1S spectra deconvoluted into four peaks 398.2, 399.8, 400.8 and 402.2 eV corresponding to pyridinic-N, pyrrolic-N, graphitic-N and oxygenated pyridinic nitrogen (NO_x) [62–64].

The average % concentration of the different N-configuration in N1s is summarized in Supplementary Table S2.

The NPAC-0.5 was comprised of 37% pyridinic-N, 56.7% pyrrolic-N and 1.3 % graphitic-N and 5% NO_X while NPAC-1 had of 40% pyridinic-N, 31% pyrrolic-N and 28% graphitic-N and 1% NO_X. The high percentage of pyridinic-N and pyrrolic-N indicates that the nitrogen atoms are bonded to the edges of carbon and sp^3 hybridized carbon. The NPAC-0.5 material possessed the lowest graphitic N and highest NO_X among all N doped samples meaning that most of the nitrogen atoms reside on the edges as oxygenated nitrogen groups. However, the NPAC-1 sample displayed the lowest NO_X suggesting that the majority of the nitrogen atoms were incorporated inside the carbon matrix and not on the edges. In contrast, the NPAC-2 sample had the highest graphitic-N content (31.5%) and a relatively higher NO_X content (3.8%) as compared to the NPAC-1. The high percentage of graphitic-N can be ascribed to the replacement of the carbon by nitrogen atoms within the carbon lattice during the *ex-situ doping* process. The deconvolution of the O1s core level spectra (Fig. S2 (d- f)) show three peaks at 530.5, 531.7 and 533.0 eV which can be assigned to C-O or, C=O/N-O and O-C=O bonds, respectively [65,66].

The XPS analysis clearly shows that the atomic composition of the NPAC samples is greatly

influenced by the mass ratio of PS:KOH. The surface chemistry of the NPAC materials plays a major role in determining their physical, structural and electrochemical properties. Specifically, the various nitrogen configurations in the N-doped carbons are known to play a vital role in improving the material's electrochemical performance [33]. The pyridinic and pyrrolic nitrogen aid in increasing the overall amount of charge stored due to the enhanced charge accumulation on the electrolyte/electrode interface and surface wettability of the electrodes [67]. Meanwhile, the graphitic N and the oxidized pyridinic-N can enhance the electron transport which improves the electrode materials' electrical conductivity [33,64].

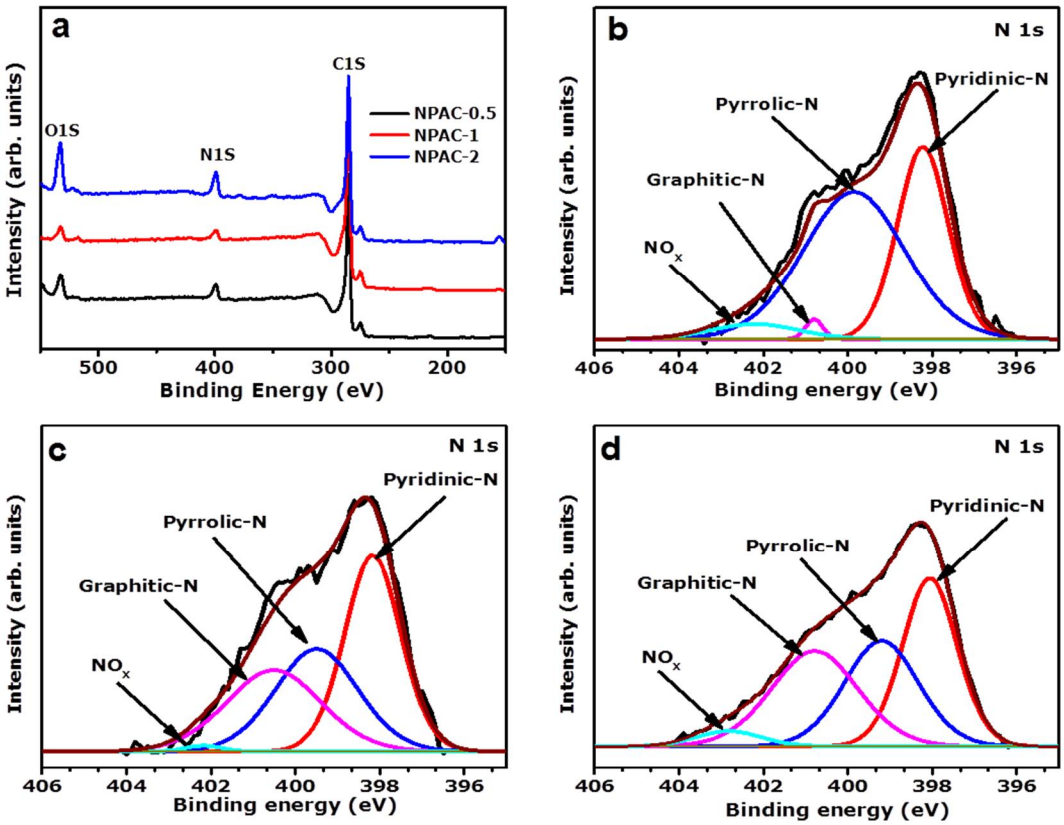

Fig. 4. (a) XPS survey spectra of the N doped samples and XPS spectra of deconvoluted N1s peaks, (b) NPAC-0.5, (c) NPAC-1 and (d) NPAC-2 materials.

3.3 Electrochemical analysis

To evaluate the electrochemical performance of the PACs and NPACs, the electrodes materials were firstly performed in half-cell configuration as shown in Fig. 5. Fig. 5(a-b) show the cyclic

voltammetry (CV) plots at a scan rate of 40 mV s^{-1} for the PACs and NPACs, respectively with different KOH mass ratios in both positive and negative potential window. All the CV curves exhibited a quasi-rectangular shape revealing an electric double layer (EDL) capacitive behaviour in both positive (0.0 - 0.9 V) and negative (-1.0 - 0.0V) operating potential windows. A slight difference was noticed in the CV curve in positive potential for PAC-1 compared to the other samples. The observed abnormality in the sample's CV curve suggests some difficulties in charge propagation resulting in the somewhat resistive behavior of its voltammogram [68]. Nevertheless, the PAC-1 still preserved the highest value of current response, being remarkably higher than for PAC-0.5 and PAC-2. The PAC-1 and NPAC-1 electrodes displayed a quasi-rectangular CV profile with a higher current response in both operating potentials as compared to the PAC and NPAC at other KOH mass concentrations. This higher current response could be attributed to the enhanced porous network, reactive carbon material surface and the presence of nitrogen atom from *ex-situ doping* which aids in charge accumulation and ions transport at the electrode/electrolyte interface.

The galvanostatic charge discharge (GCD) profiles for all the working material electrodes displayed a symmetrical triangular characteristic with a small IR drop at 1 A g^{-1} specific current within a potential range of -1.0 - 0.0 V and 0.0 - 0.9 V as seen in Fig. S4(a-d). This triangular behaviour confirms the typical double layer capacitive nature of the carbon materials as seen from the CV curves. The storage mechanism in this study exhibits a clear EDLC signature with a rectangular-like CV and quasi-symmetric GCD curve with respect to potential as a function of discharge time. The quasi-behavior is linked to some pseudocapacitance contribution from the functional groups on the carbon surface. The specific capacitance (C_s) as-calculated from the slope of the discharge section of the GCD profiles using Eq. (1) in the positive and negative operating potential windows is presented in Figs. 5 and S4 (e-f). Fig. 5(c-d) depicted the C_s of the PAC and NPAC electrodes materials in the negative potential window of -1.0 - 0.0 V while Fig. S4 (e-f) displayed the C_s in the positive potential ranging from 0.0 to 0.9 V as function of

the specific current ranging from 1 to 10 A g^{-1}. As clearly observed in these figures, the PAC-1 and NPAC-1 exhibited higher C_s values of 167 F g^{-1} and 216 F g^{-1}, respectively at 1 A g^{-1}. These values demonstrate that after nitrogen doping the specific capacitance of the PAC-1 electrode was improved appreciably by 30% of the pristine value which agrees with the higher current response recorded in the CV profiles. In addition, the low C_s of the PAC-2 and NPAC-2 electrodes (80.77 F g^{-1} and 76.4 F g^{-1}, respectively) could be attributed to the low specific surface area ($\sim$ 500 m^2 g^{-1}) resulting from the free carbon and nitrogen atoms that covered the pores which limits the ion diffusion into the porous carbon.

Electrochemical impedance spectroscopy (EIS) was tested to further investigate ion diffusion and transport kinetics of the pristine and N-doped PAC electrodes. Fig. 5(e-f) shows the Nyquist plot of the pristine and N doped PACs material electrodes.

All the electrode materials displayed a vertical line slightly deviated from the –*Z*" axis (imaginary impedance axis) at low frequency demonstrating an ideal capacitive behaviour. At high frequency, the intersection with the real *Z*' axis represents the equivalent series resistance (ESR) which consists of the intrinsic resistance within the electrolyte, resistance at electrolyte/electrode interface and contact resistance between electrode and current collector [69]. The presence of the semi-circle at the high to mid frequency reveals the charge transfer resistance (R_{ct}) due to the presence of the functional groups on the surface of the carbon material [70]. From Fig. 5(e and f), it is clearly observed that the presence of nitrogen in the carbon matrix reduce the ESR and R_{ct} values of the PAC-0.5 and PAC-1 (inset to the Fig. 5(e-f)) which indicating a fast ions transport into the electrode-electrolyte interface and less resistance between the electrode and current collector. The ESR of the PAC-2 increased after the incorporation of the nitrogen into the carbon network from 0.48 Ω to 0.52 Ω due to the oxygen and nitrogen containing groups which increase the resistance of the electrode materials. For all the electrodes materials, PAC-1 and NPAC-1 electrodes displayed the low internal

resistance values which can be ascribed to the presence of fewer oxygen containing groups and an abundant porous network enabling better accessibility of the pores to the electrolyte ions as compared to the other PAC and NPAC electrodes. A similar trend was observed by Hulicova-Jurcakova et al. where carbons with less oxygenated functional groups gave lower internal resistance than carbons with higher oxygen-containing [6]. Moreover, the NPAC-1 electrode showed a shorter diffusion length and smaller R_{ct} among the other electrodes as observed from the Nyquist plot. This smaller R_{ct} and the shorter diffusion length are associated with the good surface wettability from the electrode-electrolyte interactions and the ion kinetic into the electrode pores, respectively.

In general, the N PAC-1 electrode exhibited a relatively better electrochemical performance as compared to the other doped and pristine material electrodes. Incorporating the nitrogen atom (via *ex-situ*-doping) into the carbon matrix with a moderate quantity of KOH delivered abundant electrochemically-active sites on the material electrode surface, which could create a good interfacial contact between the electrode and electrolyte for ion dynamics. The electrochemical performance of the NPAC-1 electrode is linked to their high degree of disorder (I_D/I_G ratio), resulting in their high degree of amorphous carbon state which provided good surface hydrophilicity and surface wettability. Additionally, the high specific surface area and the large pore size distribution of the material are favourable for easy ion diffusion to the active electrode surface.

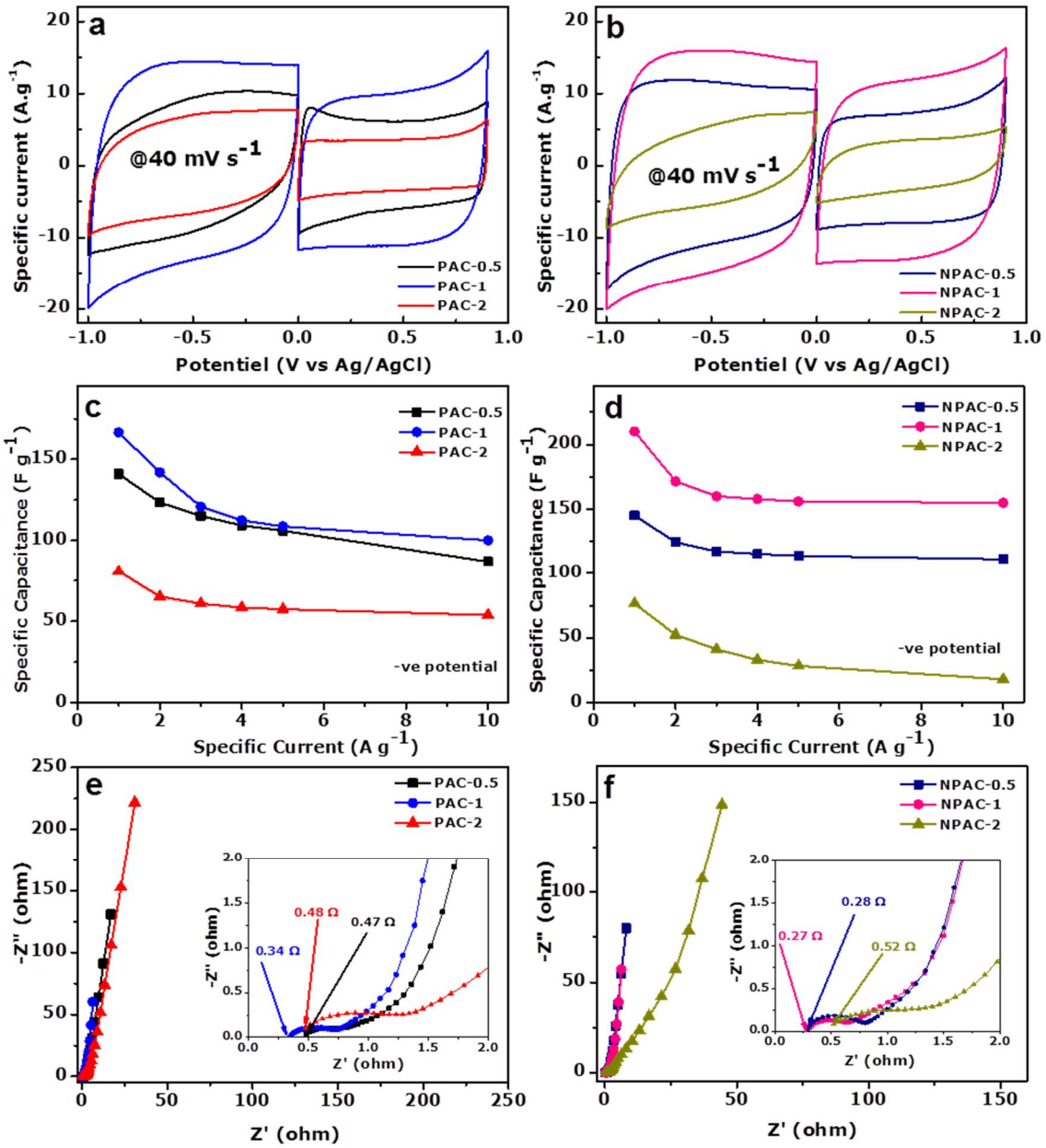

Fig. 5. Electrochemical performance of the pristine and N-doped PACs in a three-electrode configuration: (a and b) Cyclic voltammetry at scan rate of 40 mV s-1, (c and d) specific capacitance at various gravimetric current values and (e and f) Nyquist plots.

Subsequently, a symmetric device was assembled using the NPAC-1 samples as both positive and negative electrodes using the same electrolyte 2.5 M KNO_3.

Fig. 6(a) displays the cyclic voltammetry (CV) curves of the NPAC-1//NPAC-1 device in a two-electrode cell fixture at different scan rates from 10 to 500 mV s^{-1}.

The CV curves show a rectangular-like shape which indicates an ideal capacitive behaviour in

an extended voltage window of up to 2.0 V. The rectangular-like behaviour is still maintained even at high scan rate of 0.5 V s^{-1} which reveals a good rate capability and also rapid ion diffusion [71]. The galvanostatic charge discharge (GCD) profiles at various specific current values (1 - 20 A g^{-1}) for the NPAC-1//NPAC-1 device are shown in Fig. 6(b). All the GCD profiles exhibit a quasi-symmetric triangular pattern with a small IR drop suggesting an excellent charge-discharge reversibility and good double layer capacitive charge storage in the assembled symmetric supercapacitor. Fig. 6(c) represents the specific capacitance of the device at different specific currents calculated from the GCD profiles using equation (2). It has been seen that the *ex-situ-doped* NPAC-1//NPAC-1 possesses a relatively high specific capacitance per electrode (C_{el}) of 251.2 F g^{-1} at 1 A g^{-1}. A C_{el} value of 158.4 F g^{-1} was still retained even at a high specific current of 20 A g^{-1} demonstrating a good electrode rate capability. Such C_{el} value is comparable with those results reported in the literature on nitrogen doped carbon materials from biomass [72–75].

The electrochemical impedance spectroscopy (EIS) was also carried out on the as-fabricated NPAC-1//NPAC-1 symmetric device. Fig. 6(d) presents the Nyquist plot of the symmetric cell which exhibited an almost linear vertical line in low frequency. This confirms the ideal EDLC behaviour as seen from the CV and GCD curves. The inset of Fig. 6(d) showed the ESR and R_{ct} of 0.79 Ω and 0.17 Ω, respectively. These small values are an indication of fast ion transport and good charge transfer process within the electrodes. Fig. 6(e) exhibited the Bode curve of the symmetric device which displayed the plot of the phase angle against the frequency. It can be seen that at low frequency region, the phase angle of the cell is - 87 ° close to an ideal capacitor of -90 °. This result of the cell device suggested a low ion diffusion resistivity [76]. In Fig. 6(f), the complex capacitance ($C(\omega)$) of the as-prepared device was plotted as a function of the frequency.

The complex capacitance $C(\omega)$ represents the real part and the imaginary part of the complex

capacitance and was determined by using the Eqs. below [77,78].

$$C(\omega) = C'(\omega) - jC"(\omega) \quad (5)$$

$$C'(\omega) = \frac{-Z"(\omega)}{\omega|Z(\omega)|^2} \quad (6)$$

$$C"(\omega) = \frac{Z\prime(\omega)}{\omega|Z(\omega)|^2} \quad (7)$$

where $Z'(\omega)$ and $Z"(\omega)$ represent the real and imaginary part of the complex impedance $Z(\omega)$ respectively given by $Z(\omega) = Z'(\omega) - jZ"(\omega)$, ω is the angular frequency ($\omega = 2\pi f$).

At low frequency, the real part of the complex capacitance $C'(\omega)$ corresponds to the capacitance delivered of the cell measured via constant-current discharge. While the imaginary part of the capacitance, $C"(\omega)$ is related to the energy loss by dissipation during irreversible process at electrode/electrolyte interface [79,80]. From Fig. 6(f), the $C'(\omega)$ decreases gradually when the frequency increases. On the other hand, the $C"(\omega)$ versus frequency exhibit a maximum peak at a frequency f_0 of 1.1 Hz corresponding to the relaxation time τ_0 of the device. τ_0 is defined by $1/2\pi f_0$ which represented the minimum time required to charge the symmetric cell [81]. The device shows a small constant time of 0.87 s which indicated the symmetric cell can be fully charged within a relatively short period of time. This small value of the relaxation time suggests also a good electrical conductivity as well as a higher pores accessibility for fast ions transport into the electrode/electrolyte interface [82]. These results could be attributed to the synergistic effect of the nitrogen doping and improved surface porosity of the porous carbon matrix.

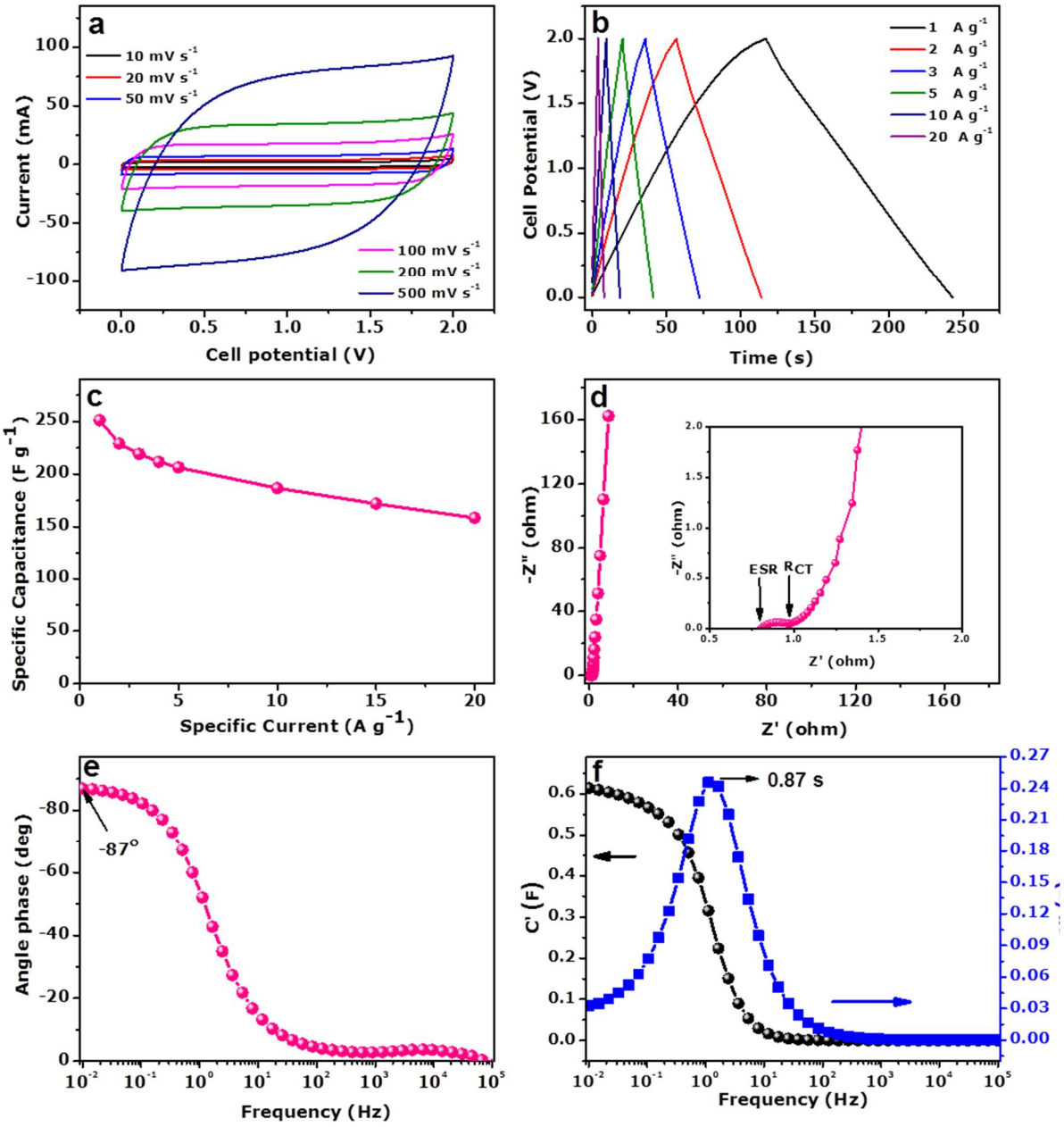

Fig. 6. Electrochemical performance of the NPAC-1// NPAC-1 symmetric device: (a) Cyclic voltammetry at different scan rates, (b) galvanostatic charge-discharge plots at various specific current, (c) specific capacitance as a function of specific current, (d) Nyquist plots, (e) Bode plot and (f) capacitance C' and C" variation as a function of frequency

Fig. 7(a) displays the Ragone plot of the NPAC-1//NPAC-1 symmetric supercapacitor. The fabricated device delivers a specific energy of 35 Wh kg^{-1} corresponding to a specific power of 1 kW kg^{-1} at specific current of 1 A g^{-1}.

Moreover, the specific energy was still maintained at 22 Wh kg^{-1} with a specific power of 20

kW kg^{-1} even at high specific current of 20 A g^{-1}. These values of the specific energy and specific power for the NPAC-1//NPAC-1 device are higher than most recently reported values in the literature on nitrogen doped activated carbon derived from biomass as shown in Table 3. and Fig. 7(a). Until now, limited reports exist in the literature on biomass-based nitrogen doped activated carbon from using KNO_3 electrolyte. Hui and co-workers [83] reported the nitrogen-doped porous carbon nanosheets from pomelo mesocarps (N-PMNC). The preparation of the N-PMNC was done by an *in-situ doping* procedure by mixing the pomelo mesocarps with $CaCl_2$ and urea. The symmetric device fabricated possesses a specific energy of 14.7 kW kg^{-1} with specific power of 90 W kg^{-1} in 0.5 M Na_2SO_4 at 0.25 A g^{-1} specific current. Recently, Hao *et al.* [84] synthesized a porous nitrogen-doped orange peel (PN-OPNC) by an *in situ-doping* method using $FeCl_3$ and urea as activating agent and nitrogen source, respectively. The PN-OPNC//PN-OPNC symmetric device was tested in a potential window of 1.6 V using 0.5 M Li_2SO_4 electrolyte. The device exhibited a specific energy of 16 kW h kg^{-1} with specific power of 400 W kg^{-1} at specific current of 0.5 A g^{-1}. Donglin and co-authors [41] prepared a 3D nitrogen-doped porous carbon (3DNPC) via two steps by pyrolyzing the mixture taro stems with KOH followed by an *post doping* with melamine. The specific energy of the symmetric cell was 5.56 Wh kg^{-1} with a specific power of 5 000 W kg^{-1} in polyvinyl alcohol (PVA)/KOH as electrolyte at 10 A g^{-1}. The good electrochemical performance of the NPAC-1//NPAC-1 could be ascribed to the good surface chemistry of the porous carbon material with a moderate mass ratio of the KOH followed by the incorporation of the nitrogen atom in the carbon matrix. The cycling stability of the symmetric device was evaluated after continuous charging and discharging of the device over several cycles (~ 20 000) at specific current of 5 A g^{-1}. As observed in Fig. 7(b), the symmetric cell exhibits a columbic efficiency of 99% and a capacitance retention of 83.3% after 20 000 constant galvanostatic cycles. The observed sharp drop in capacitance at around 4000 cycles of cycling test is due to the electrochemical degradation of the electrode material as a result of the wide operating potential (2.0 V) and

Table 3. Comparison of the electrochemical performance of nitrogen doped activated carbon from biomass

Raw Materials	Precursors	Electrolyte	Operating Potential windows	Specific current ($A\ g^{-1}$)	Specific energy ($Wh\ kg^{-1}$)	Specific power (Wkg^{-1})	Ref
			In-situ doping				
Pomelo mesocarps	$CaCl_2$/ urea	0.5 M Na_2SO_4	1.8 V	0.25	14.7	90	[83]
Orange peel	$FeCl_3$/urea	0.5 M Li_2SO_4	1.6 V	0.5	16	400	[84]
Pine Nut shell	KOH/melamine	1 M Na_2SO_4	1.8 V	1	11.9	463.6	[72]
Dumpling flour	KOH/urea	6M KOH	1.2 V	0.5	15.92	358.28	[87]
Cauliflower	KOH/imidazole dinone	1 M Na_2SO_4	1.8 V	0.5	20.5	448.8	[88]
Pueraria	K_2CO_3/ melamine	6M KOH	1 V	0.5	8.46	123	[75]
Cellulose	NaOH/urea	1 M Na_2SO_4	1.8 V	0.5	17.24	452	[89]
Cycas leaves	KOH/urea	6 M KOH	1 V	0.5	9.13	125	[90]
Peanut shell	KOH/urea	2.5 M KNO_3	1.8 V	1	25.2	900	[38]
			Ex-situ doping				
Taro stems	KOH/melamine	PVA/KOH	1 V	10	5.56	5000	[41]
Ginkgo leaves	KOH+ K_2CO_3/ureophil	6 M KOH	1 V	0.5	7.8	241.1	[91]
Peanut shell	**KOH/melamine**	**2.5 M KNO_3**	**2 V**	**1** **10**	**34.9** **25.9**	**1000** **10000**	**This work**

high specific current applied to the device [85]. Nonetheless, the device was observed to become stable after about 7000 cycles and could maintain this stable condition even for a very large cycle number of over 20 000 cycles. Fig. S5(a-b) in supporting information reveals the comparison of the CV curves and Nyquist plot of the device before and after the cycling of over 20000 cycles. The CV curves of the cell at a scan rate 40 mV s^{-1} (Fig. S5(a)) show a similar behaviour with no significant level of degradation. These could be due to consumption of some of the active sites in the electrode material that results in some subsequent capacitance

loss [86]. An increase of the ESR and R_{ct} values of 1.07Ω and 0.21Ω from the initials values has been observed in Fig. S5(b). These small increases and the shorter diffusion length demonstrated that NPAC-1 electrode did not deteriorate significantly after the cycling stability.

The notable stability of the cell can be confirmed after investigating the specific capacitance for each floating test (voltage holding) as shown in Fig. 7(c). The floating test analysis showed the specific capacitance for each 10 h period of holding at a maximum operating cell voltage (2.0 V) for 180 h. Fig. 7(c) shows a specific capacitance increase for the first 60 h of floating after which the specific capacitance was retained constant value for the next 120 h.

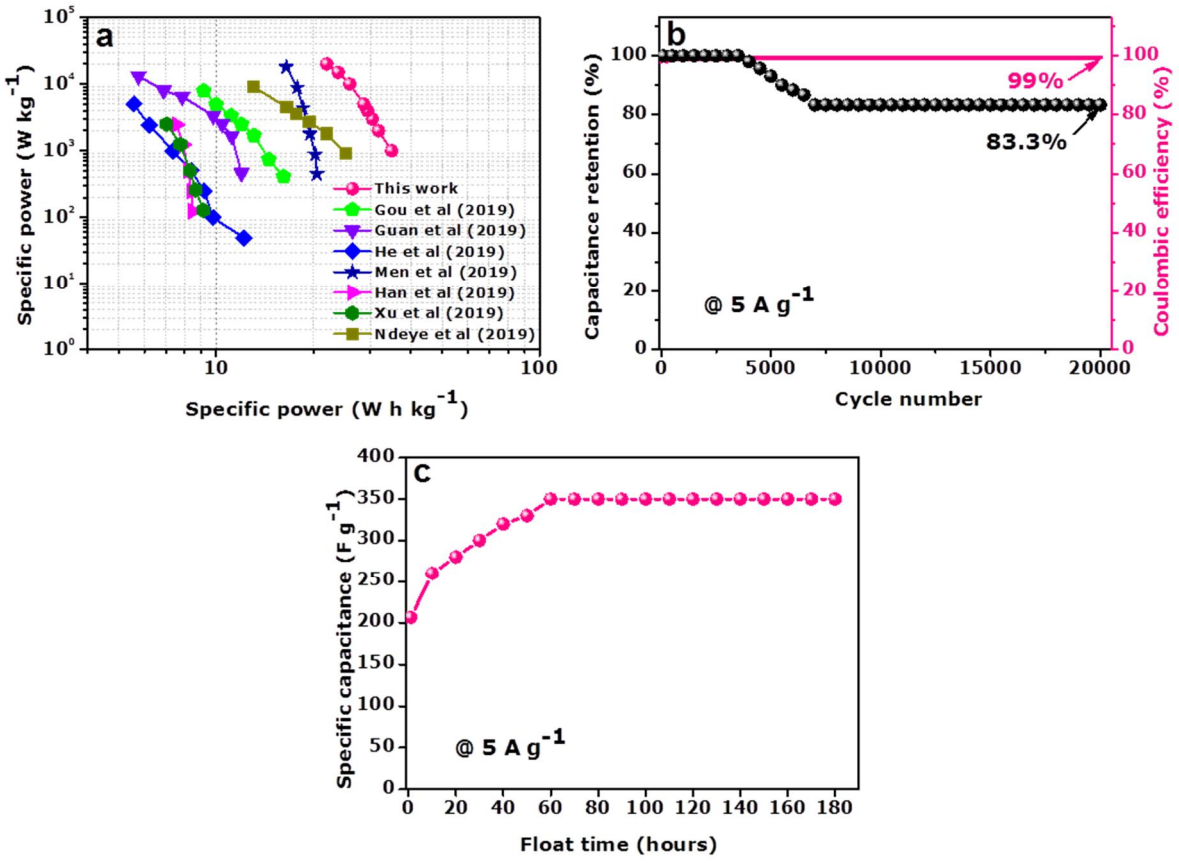

Fig. 7.(a) Ragone plot for the NPAC-1//NAPC-1 device, (b) Columbic efficiency and specific capacitance retention vs. cycle number and (c) specific capacitance as function of voltage holding time for a period of 180 h.

The increased specific capacitance value for the device can be ascribed to the opening of small pores, surface wettability and enhanced surface interaction of the electrode ions with the carbon electrode upon voltage holding. The large micropore of the NPAC-1 play a role in the charging of the double layer capacitor and the mesopores volume provide charge propagation pathways during process. The surface functionalities on the NPAC-1 influence the surface chemistry and interactions of the electrolyte ions with the carbon electrode leading to lower electrolyte ion resistance and improved charge storage capability during the voltage holding process. In addition, the excellent capacitance retention portrayed by the NPAC-1 electrode material reveals a stable electrolyte ion interaction with the carbon surface. Thus the voltage holding test is beneficial for pore opening and faster ion transport and charge storage.

The specific capacitance of the symmetric device was enhanced to 350 F g^{-1} by 69.5% from the initial value of 206.4 F g^{-1} up to 180 h (1 week and 12 h) holding time at 5 A g^{-1}. This improvement is also emphasized with an increase in the device specific energy value from 28.7 to 48.6 Wh kg^{-1} after the floating test. Noteworthy, the specific energy of the cell obtained after holding test at 5 A g^{-1} is higher than that of the cell at 1 A g^{-1} (35 W h kg^{-1}) before the holding test. Thus, this device demonstrated an excellent electrochemical stability over a long period of time (~7+ days) in 2.5 M KNO_3 aqueous electrolyte.

4. **Conclusion**

Ex-situ nitrogen-doped porous carbons have been successfully prepared through two steps process: chemical activation of the peanut shell with different mass ratios of KOH as an activating agent followed by nitrogen-doping with melamine. The experimental results obtained show the effect of the mass loading of activating agents on the properties of ex-situ N-doped activated carbon. The nitrogen-doped carbon yielded with the optimum mass ratio of 1:1 (PS:KOH) was found to be the best electrode material which displayed a high specific

surface area of 1442 m^2 g^{-1} and varying nitrogen configurations (40% pyridinic-N, 31% pyrrolic-N, 28% graphitic-N and 1% NO_X). The assembled supercapacitor (NPAC-1//NPAC-1) based on the *ex-situ* nitrogen-doped peanut shell activated carbon electrode showed an excellent specific energy and power of 34.9 Wh kg^{-1} and 1 kW kg^{-1}, respectively in a wide potential range of 2.0 V with a capacitance retention of 83.2% up to 20 000 cycles. NPAC-1//NPAC-1 also presented good stability through voltage holding analysis up to 180 h displaying a high specific capacitance and specific energy which demonstrated that the cell device performed better after the voltage holding test. This study revealed that the *ex-situ* nitrogen-doped porous carbon process is a promising and sustainable route for the synthesis of relatively high nitrogen content N-doped AC for outstanding energy storing capability.

Acknowledgement

This research was funded by the South African Research Chairs Initiative (SARChI) of the Department of Science and Technology and the National Research Foundation (NRF) of South Africa (Grant No. 61056). Any idea, finding, conclusion or recommendation expressed in this publication is that of the author(s). The NRF does not accept any liability in this regard. N. F. Sylla acknowledges NRF through SARChI in Carbon Technology and Materials and the University of Pretoria for financial support.

References

[1] C. Vix-Guterl, E. Frackowiak, K. Jurewicz, M. Friebe, J. Parmentier, F. Béguin, Electrochemical energy storage in ordered porous carbon materials, Carbon. 43 (2005) 1293–1302.

[2] J. Chmiola, G. Yushin, Y. Gogotsi, C. Portet, P. Simon, P.L. Taberna, Anomalous increase in carbon at pore sizes less than 1 nanometer, Science. 313 (2006) 1760–1763.

[3] S. Dutta, A. Bhaumik, K.C.W. Wu, Hierarchically porous carbon derived from polymers and biomass: Effect of interconnected pores on energy applications, Energy and Environmental

Science. 7 (2014) 3574–3592.

[4] P. Simon, Y. Gogotsi, Charge storage mechanism in nanoporous carbons and its consequence for electrical double layer capacitors, Trans. R. Soc. A. 368 (2010) 3457–3467.

[5] C. Merlet, B. Rotenberg, P.A. Madden, P.-L. Taberna, P. Simon, Y. Gogotsi, M. Salanne, On the molecular origin of supercapacitance in nanoporous carbon electrodes, Nature Materials. 11 (2012) 306–310.

[6] F.O. Ochai-Ejeh, A. Bello, J. Dangbegnon, A.A. Khaleed, M.J. Madito, F. Bazegar, N. Manyala, High electrochemical performance of hierarchical porous activated carbon derived from lightweight cork (Quercus suber), Journal of Materials Science. 52 (2017) 10600–10613.

[7] D. Momodu, N.F. Sylla, B. Mutuma, A. Bello, T. Masikhwa, S. Lindberg, A. Matic, N. Manyala, Stable ionic-liquid-based symmetric supercapacitors from Capsicum seed porous carbons, Journal of Electroanalytical Chemistry. 838 (2018) 119–128.

[8] D. Puthusseri, V. Aravindan, S. Madhavi, S. Ogale, 3D micro-porous conducting carbon beehive by single step polymer carbonization for high performance supercapacitors: The magic of in situ porogen formation, Energy and Environmental Science. 7 (2014) 728–735.

[9] B. Moyo, D. Momodu, O. Fasakin, A. Bello, J. Dangbegnon, N. Manyala, Electrochemical analysis of nanoporous carbons derived from activation of polypyrrole for stable supercapacitors, Journal of Materials Science. 53 (2018) 5229–5241.

[10] W. Bao, A.K. Mondal, J. Xu, C. Wang, D. Su, G. Wang, 3D hybrid-porous carbon derived from carbonization of metal organic frameworks for high performance supercapacitors, Journal of Power Sources. 325 (2016) 286–291.

[11] W. Teng, N. Bai, Z. Chen, J. Shi, J. Fan, W. xian Zhang, Hierarchically porous carbon derived from metal-organic frameworks for separation of aromatic pollutants, Chemical Engineering Journal. 346 (2018) 388–396.

[12] S. Wang, T. Wang, P. Liu, Y. Shi, G. Liu, J. Li, Hierarchical porous carbons derived from microporous zeolitic metal azolate frameworks for supercapacitor electrodes, Materials Research Bulletin. 88 (2017) 62–68.

[13] Y. Lei, M. Gan, L. Ma, M. Jin, X. Zhang, G. Fu, P. Yang, M. Yan, Synthesis of nitrogen-doped porous carbon from zeolitic imidazolate framework-67 and phenolic resin for high performance supercapacitors, Ceramics International. 43 (2017) 6502–6510.

[14] P.T. Williams, A.R. Reed, Development of activated carbon pore structure via physical and chemical activation of biomass fibre waste, Biomass and Bioenergy. 30 (2006) 144–152.

[15] H. Lu, K. Kim, Y. Kwon, X. Sun, R. Ryoo, X.S. Zhao, Zeolite-templated nanoporous carbon for high-performance supercapacitors, Journal of Materials Chemistry A. 6 (2018) 10388–10394.

[16] W. Yang, W. Yang, F. Ding, L. Sang, Z. Ma, G. Shao, Template-free synthesis of ultrathin porous carbon shell with excellent conductivity for high-rate supercapacitors, Carbon. 111 (2017) 419–427.

[17] C. Wang, D. Ma, X. Bao, Transformation of Biomass into Porous Graphitic Carbon Nanostructures by Microwave Irradiation, The Journal of Physical Chemistry C. 112 (2008) 17596–17602.

[18] M. Seredych, D. Hulicova-Jurcakova, G.Q. Lu, T.J. Bandosz, Surface functional groups of carbons and the effects of their chemical character, density and accessibility to ions on electrochemical performance, Carbon. 46 (2008) 1475–1488.

[19] D. Hulicova-Jurcakova, M. Seredych, G.Q. Lu, T.J. Bandosz, Combined effect of nitrogen- and oxygen-containing functional groups of microporous activated carbon on its electrochemical performance in supercapacitors, Advanced Functional Materials. 19 (2009) 438–447.

[20] X. Wu, X. Hong, Z. Luo, K.S. Hui, H. Chen, J. Wu, K.N. Hui, L. Li, J. Nan, Q. Zhang, The effects of surface modification on the supercapacitive behaviors of novel mesoporous carbon derived from rod-like hydroxyapatite template, Electrochimica Acta. 89 (2013) 400–406.

[21] P. Cheng, S. Gao, P. Zang, X. Yang, Y. Bai, H. Xu, Z. Liu, Z. Lei, Hierarchically porous carbon by activation of shiitake mushroom for capacitive energy storage, Carbon. 93 (2015) 315–324.

[22] L. Wang, R. Wang, H. Zhao, L. Liu, D. Jia, High rate performance porous carbon prepared from coal for supercapacitors, Materials Letters. 149 (2015) 85–88.

[23] J. Li, K. Han, J. Qi, Z. Teng, M. Li, M. Wang, Biomass-derived 3D hierarchical porous carbon by two-step activation method for supercapacitor, Journal of Materials Science: Materials in Electronics. 21 (2019) 19415-19425.

[24] N.D. Kim, W. Kim, J.B. Joo, S. Oh, P. Kim, Y. Kim, J. Yi, Electrochemical capacitor performance of N-doped mesoporous carbons prepared by ammoxidation, Journal of Power Sources. 180 (2008) 671–675.

[25] W. Yang, W. Yang, L. Kong, A. Song, X. Qin, G. Shao, Phosphorus-doped 3D hierarchical porous carbon for high-performance supercapacitors: A balanced strategy for pore structure and chemical composition, Carbon. 127 (2018) 557–567.

[26] S. Yaglikci, Y. Gokce, E. Yagmur, Z. Aktas, The performance of sulphur doped activated carbon supercapacitors prepared from waste tea, Environmental Technology. 41 (2020) 36-48.

[27] J. Li, X. Li, D. Xiong, L. Wang, D. Li, Enhanced capacitance of boron-doped graphene aerogels for aqueous symmetric supercapacitors, Applied Surface Science. 475 (2019) 285–293.

[28] W. Yang, W. Yang, L. Kong, A. Song, X. Qin, Facile synthesis of nitrogen-doped porous carbon for high-performance supercapacitors, 7 (2017) 55257–55263.

[29] L.-F. Chen, X.-D. Zhang, H.-W. Liang, M. Kong, Q.-F. Guan, P. Chen, Z.-Y. Wu, S.-H. Yu, Synthesis of Nitrogen-Doped Porous Carbon Nanofibers as an Efficient Electrode Material for Supercapacitors, ACS Nano. 6 (2012) 7092–7102.

[30] W. Du, X. Wang, X. Sun, J. Zhan, H. Zhang, X. Zhao, Nitrogen-doped hierarchical porous carbon using biomass-derived activated carbon/carbonized polyaniline composites for

supercapacitor electrodes, Journal of Electroanalytical Chemistry. 827 (2018) 213–220.

[31] S. Li, Z. Fan, Nitrogen-doped carbon mesh from pyrolysis of cotton in ammonia as binder-free electrodes of supercapacitors, Microporous and Mesoporous Materials. 274 (2019) 313–317.

[32] C. Kim, C. Zhu, Y. Aoki, H. Habazaki, Heteroatom-doped porous carbon with tunable pore structure and high specific surface area for high performance supercapacitors, Electrochimica Acta. 314 (2019) 173–187.

[33] Y. Deng, Y. Xie, K. Zou, X. Ji, Review on recent advances in nitrogen-doped carbons: preparations and applications in supercapacitors, Journal of Materials Chemistry A. 4 (2016) 1144–1173.

[34] N. Deka, J. Barman, J. Deka, K. Raidongia, G.K. Dutta, Microporous Organic Polymer-Derived Nitrogen-Doped Porous Carbon Spheres for Efficient Capacitive Energy Storage, ChemElectroChem. 6 (2019) 3327–3336.

[35] L. Niu, C. Shen, L. Yan, J. Zhang, Y. Lin, Y. Gong, C. Li, C.Q. Sun, S. Xu, Waste bones derived nitrogen–doped carbon with high micropore ratio towards supercapacitor applications, Journal of Colloid and Interface Science. 547 (2019) 92–101.

[36] N. Zdolšek, R.P. Rocha, J. Krstić, T. Trtić-Petrović, B. Šljukić, J.L. Figueiredo, M.J. Vujković, Electrochemical investigation of ionic liquid-derived porous carbon materials for supercapacitors: pseudocapacitance versus electrical double layer, Electrochimica Acta. 298 (2019) 541–551.

[37] X. Hu, Y.H. Wang, B. Ding, X. Wu, A novel way to synthesize nitrogen doped porous carbon materials with high rate performance and energy density for supercapacitors, Journal of Alloys and Compounds. 785 (2019) 110–116.

[38] N.F. Sylla, N.M. Ndiaye, B.D. Ngom, D. Momodu, M.J. Madito, B.K. Mutuma, & N. Manyala, Effect of porosity enhancing agents on the electrochemical performance of high-energy ultracapacitor electrodes derived from peanut shell waste, Scientific Reports. 9 (2019) 13673.

[39] L. Chen, T. Ji, L. Mu, J. Zhu, Cotton fabric derived hierarchically porous carbon and nitrogen doping for sustainable capacitor electrode, Carbon. 111 (2017) 839–848.

[40] X. Yu, J. Zhao, R. Lv, Q. Liang, C. Zhan, Y. Bai, Z.H. Huang, W. Shen, F. Kang, Facile synthesis of nitrogen-doped carbon nanosheets with hierarchical porosity for high performance supercapacitors and lithium-sulfur batteries, Journal of Materials Chemistry A. 3 (2015) 18400–18405.

[41] D. He, W. Zhao, P. Li, Z. Liu, H. Wu, L. Liu, K. Han, L. Liu, Q. Wan, F.K. Butt, X. Qu, Bifunctional biomass-derived 3D nitrogen-doped porous carbon for oxygen reduction reaction and solid-state supercapacitor, Applied Surface Science. 465 (2019) 303–312.

[42] M.D. Stoller, R.S. Ruoff, Best practice methods for determining an electrode material's performance for ultracapacitors, Energy and Environmental Science. 3 (2010) 1294–1301.

[43] S.T. Senthilkumar, R.K. Selvan, Y.S. Lee, J.S. Melo, Electric double layer capacitor and its improved specific capacitance using redox additive electrolyte, J. Mater. Chem. A. 1 (2013) 1086–1095.

[44] A. Bello, N. Manyala, F. Barzegar, A.A. Khaleed, D.Y. Momodu, J.K. Dangbegnon, Renewable pine cone biomass derived carbon materials for supercapacitor application, RSC Advances. 6 (2016) 1800–1809.

[45] G. Singh, K.S. Lakhi, K. Ramadass, C.I. Sathish, A. Vinu, High-Performance Biomass-Derived Activated Porous Biocarbons for Combined Pre-and Post-Combustion CO 2 Capture, ACS Sustainable Chem. Eng. 7 (2019) 7412−7420.

[46] H. Teng, L.-Y. Hsu, High-Porosity Carbons Prepared from Bituminous Coal with Potassium Hydroxide Activation, Ind. Eng. Chem. Res. 38 (1999) 2947–2953.

[47] H. Wang, Q. Gao, J. Hu, High Hydrogen Storage Capacity of Porous Carbons Prepared by Using Activated Carbon, J. AM. CHEM. SOC. 131 (2009) 7016–7022.

[48] H. Xiong, M.A. Motchelaho, M. Moyo, L.L. Jewell, N.J. Coville, Fischer-Tropsch synthesis: Iron-based catalysts supported on nitrogen-doped carbon nanotubes synthesized by post-doping, Applied Catalysis A: General. 482 (2014) 377–386.

[49] M. Song, Y. Zhou, X. Ren, J. Wan, Y. Du, G. Wu, F. Ma, Biowaste-based porous carbon for supercapacitor: The influence of preparation processes on structure and performance, Journal of Colloid and Interface Science. 535 (2019) 276–286.

[50] D. Momodu, N.F. Sylla, B. Mutuma, A. Bello, T. Masikhwa, S. Lindberg, A. Matic, N. Manyala, Stable ionic-liquid-based symmetric supercapacitors from Capsicum seed-porous carbons, Journal of Electroanalytical Chemistry. 838 (2019) 119–128.

[51] M.W. Dlamini, T.N. Phaahlamohlaka, D.O. Kumi, R. Forbes, L.L. Jewell, N.J. Coville, Post doped nitrogen-decorated hollow carbon spheres as a support for Co Fischer-Tropsch catalysts, Catalysis Today. 342 (2019) 99-110.

[52] M.J. Mostazo-López, D. Salinas-Torres, R. Ruiz-Rosas, E. Morallón, D. Cazorla-Amorós, Nitrogen-Doped Superporous Activated Carbons as Electrocatalysts for the Oxygen Reduction Reaction, Materials. 12 (2019) 1346.

[53] A. Sadezky, H. Muckenhuber, H. Grothe, R. Niessner, U. Pöschl, U. Poschl, U. Pöschl, Raman microspectroscopy of soot and related carbonaceous materials: Spectral analysis and structural information, Carbon. 43 (2005) 1731–1742.

[54] Y. Zhu, M. Chen, Y. zhang, W. Zhao, C. Wang, A biomass-derived nitrogen-doped porous carbon for high-energy supercapacitor, Carbon. 140 (2018) 404–412.

[55] S.W. Choi, J. Tang, V.G. Pol, K.B. Lee, Pollen-derived porous carbon by KOH activation: Effect of physicochemical structure on CO_2 adsorption, Journal of CO_2 Utilization. 29 (2019) 146–155.

[56] Y. Li, R. Xu, B. Wang, J. Wei, L. Wang, M. Shen, J. Yang, Enhanced N-doped Porous Carbon Derived from KOH-Activated Waste Wool: A Promising Material for Selective Adsorption of CO_2/CH_4 and CH_4/N_2, Nanomaterials. 9 (2019) 266.

[57] K. Li, W. Chen, H. Yang, Y. Chen, S. Xia, M. Xia, X. Tu, H. Chen, Mechanism of biomass activation and ammonia modification for nitrogen-doped porous carbon materials, Bioresource Technology. 280 (2019) 260–268.

[58] O. Fasakin, J.K. Dangbegnon, D.Y. Momodu, M.J. Madito, K.O. Oyedotun, M.A. Eleruja, N. Manyala, Synthesis and characterization of porous carbon derived from activated banana peels with hierarchical porosity for improved electrochemical performance, Electrochimica Acta. 262 (2018) 187–196.

[59] C. Kagenda, I. Lule, C. Paulik, Nitrogen-doped carbon materials for high performing lithium air batteries, South African Journal of Chemical Engineering. 25 (2018) 32–41.

[60] Z. Xing, Z. Ju, Y. Zhao, J. Wan, Y. Zhu, Y. Qiang, Y. Qian, One-pot hydrothermal synthesis of Nitrogen-doped graphene as high-performance anode materials for lithium ion batteries, Scientific Reports. 6 (2016) 26146.

[61] K. Zou, Y. Deng, J. Chen, Y. Qian, Y. Yang, Y. Li, G. Chen, Hierarchically porous nitrogen-doped carbon derived from the activation of agriculture waste by potassium hydroxide and urea for high-performance supercapacitors, Journal of Power Sources. 378 (2018) 579–588.

[62] Z.-H. Sheng, L. Shao, J.-J. Chen, W.-J. Bao, F.-B. Wang, X.-H. Xia, Catalyst-Free Synthesis of Nitrogen-Doped Graphene via Thermal Annealing Graphite Oxide with Melamine and Its Excellent Electrocatalysis, ACS Nano. 5 (2011) 4350–4358.

[63] B.K. Mutuma, C.I. Garcia-Martinez, R.C. Dias, B.J. Matsoso, N.J. Coville, I.A. Hümmelgen, Nitrogen-doped hollow carbon spheres as chemical vapour sensors, New Journal of Chemistry. 43 (2019) 8418–8427.

[64] Z. Song, L. Li, D. Zhu, L. Miao, H. Duan, Z. Wang, W. Xiong, Y. Lv, M. Liu, L. Gan, Synergistic design of a N, O co-doped honeycomb carbon electrode and an ionogel electrolyte enabling all-solid-state supercapacitors with an ultrahigh energy density †, Journal of Materials Chemistry A. 7 (2019) 816–826.

[65] N. Phattharasupakun, J. Wutthiprom, N. Ma, P. Suktha, M. Sawangphruk, High-performance supercapacitors of N-doped graphene aerogel and its nanocomposites with manganese oxide and polyaniline, Journal of the Electrochemical Society. 165 (2018) A1430–A1439.

[66] B. Mutuma, B. Matsoso, D. Momodu, K. Oyedotun, N. Coville, N. Manyala, Deciphering the Structural, Textural, and Electrochemical Properties of Activated BN-Doped Spherical Carbons, Nanomaterials. 9 (2019) 446..

[67] M. Antonietti, M. Oschatz, The Concept of "Noble, Heteroatom-Doped Carbons," Their Directed Synthesis by Electronic Band Control of Carbonization, and Applications in Catalysis and Energy Materials, Advanced Materials. 30 (2018) 1706836.

[68] K. Fic, G. Lota, M. Meller, E. Frackowiak, E. Environ, K. Fic, G. Lota, M. Meller, E. Frackowiak, Novel insight into neutral medium as electrolyte for high-voltage supercapacitors, Energy and Environmental Science. 5 (2012) 5842–5850.

[69] N.M. Ndiaye, N.F. Sylla, B.D. Ngom, F. Barzegar, D. Momodu, N. Manyala, High-performance asymmetric supercapacitor based on vanadium dioxide/activated expanded graphite composite and carbon-vanadium oxynitride nanostructures, Electrochimica Acta. 316 (2019) 19–32.

[70] K.O. Oyedotun, F. Barzegar, A.A. Mirghni, A.A. Khaleed, T.M. Masikhwa, N. Manyala, Examination of High-Porosity Activated Carbon Obtained from Dehydration of White Sugar for Electrochemical Capacitor Applications, ACS Sustainable Chemistry & Engineering. 7 (2019) 537–546.

[71] J. Du, L. Liu, Z. Hu, Y. Yu, Y. Zhang, S. Hou, A. Chen, Raw-Cotton-Derived N-Doped Carbon Fiber Aerogel as an Efficient Electrode for Electrochemical Capacitors, ACS Sustainable Chemistry & Engineering. 6 (2018) 4008–4015.

[72] L. Guan, L. Pan, T. Peng, C. Gao, W. Zhao, Z. Yang, H. Hu, M. Wu, Synthesis of Biomass-Derived Nitrogen-Doped Porous Carbon Nanosheests for High-Performance Supercapacitors, ACS Sustainable Chemistry and Engineering. 7 (2019) 8405–8412.

[73] W. Liu, J. Mei, G. Liu, Q. Kou, T. Yi, S. Xiao, Nitrogen-Doped Hierarchical Porous Carbon from Wheat Straw for Supercapacitors, ACS Sustainable Chemistry & Engineering. 6 (2018) 11595–11605.

[74] G. Lin, R. Ma, Y. Zhou, Q. Liu, X. Dong, J. Wang, KOH activation of biomass-derived nitrogen-doped carbons for supercapacitor and electrocatalytic oxygen reduction, Electrochimica Acta. 261 (2018) 49–57.

[75] X. Han, H. Jiang, Y. Zhou, W. Hong, Y. Zhou, P. Gao, R. Ding, E. Liu, A high performance nitrogen-doped porous activated carbon for supercapacitor derived from pueraria, Journal of Alloys and Compounds. 744 (2018) 544–551.

[76] X. Song, X. Ma, Y. Li, L. Ding, R. Jiang, Tea waste derived microporous active carbon with enhanced double-layer supercapacitor behaviors, Applied Surface Science. 487 (2019) 189–197.

[77] P.L. Taberna, P. Simon, J.F. Fauvarque, Electrochemical Characteristics and Impedance Spectroscopy Studies of Carbon-Carbon Supercapacitors, Journal of The Electrochemical Society. 150 (2003) 292–300.

[78] D. Jain, J. Kanungo, S.K. Tripathi, Performance enhancement approach for supercapacitor by using mango kernels derived activated carbon electrode with p-hydroxyaniline based redox additive electrolyte, Materials Chemistry and Physics. 229 (2019) 66–77.

[79] A.A. Silva, R.A. Pinheiro, A.C. Rodrigues, M.R. Baldan, V.J. Trava-Airoldi, E.J. Corat, Graphene sheets produced by carbon nanotubes unzipping and their performance as supercapacitor, Applied Surface Science. 446 (2018) 201–208.

[80] A. Oz, S. Hershkovitz, N. Belman, E. Tal-Gutelmacher, Y. Tsur, Analysis of impedance spectroscopy of aqueous supercapacitors by evolutionary programming: Finding DFRT from complex capacitance, Solid State Ionics. 288 (2016) 311–314.

[81] F. Barzegar, A. Bello, D. Momodu, M.J. Madito, J. Dangbegnon, N. Manyala, Preparation and characterization of porous carbon from expanded graphite for high energy density

supercapacitor in aqueous electrolyte, Journal of Power Sources. 309 (2016) 245–253.

[82] L. Deng, Y. Gu, Y. Gao, Z. Ma, G. Fan, Carbon nanotubes/holey graphene hybrid film as binder-free electrode for flexible supercapacitors, Journal of Colloid and Interface Science. 494 (2017) 355–362.

[83] H. Peng, G. Ma, K. Sun, Z. Zhang, Q. Yang, Z. Lei, Nitrogen-doped interconnected carbon nanosheets from pomelo mesocarps for high performance supercapacitors, Electrochimica Acta. 190 (2016) 862–871.

[84] H. Gou, J. He, G. Zhao, L. Zhang, C. Yang, H. Rao, Porous nitrogen-doped carbon networks derived from orange peel for high-performance supercapacitors, Ionics. 25 (2019) 4371–4380.

[85] K.O. Oyedotun, T.M. Masikhwa, S. Lindberg, A. Matic, P. Johansson, N. Manyala, Comparison of ionic liquid electrolyte to aqueous electrolytes on carbon nanofibres supercapacitor electrode derived from oxygen-functionalized graphene, Chemical Engineering Journal. 375 (2019) 121906.

[86] D.Y. Momodu, F. Barzegar, A. Bello, J. Dangbegnon, T. Masikhwa, J. Madito, N. Manyala, Simonkolleite-graphene foam composites and their superior electrochemical performance, Electrochimica Acta. 151 (2015) 591–598.

[87] J. Zhou, M. Wang, X. Li, Promising biomass-derived nitrogen-doped porous carbon for high performance supercapacitor, Journal of Porous Materials. 26 (2019) 99–108.

[88] B. Men, P. Guo, Y. Sun, Y. Tang, Y. Chen, J. Pan, P. Wan, High-performance nitrogen-doped hierarchical porous carbon derived from cauliflower for advanced supercapacitors, Journal of Materials Science. 54 (2019) 2446–2457.

[89] P. Song, X. Shen, X. He, K. Feng, L. Kong, Z. Ji, L. Zhai, G. Zhu, D. Zhang, Cellulose-derived nitrogen-doped hierarchically porous carbon for high-performance supercapacitors, Cellulose. 26 (2019) 1195–1208.

[90] C. Xu, F. Xu, L. Sun, L. Cao, F. Yu, H. Zhang, E. Yan, H. Peng, H. Chu, Y. Zou, A high-performance supercapacitor based on nitrogen-doped porous carbon derived from cycas leaves, International Journal of Electrochemical Science. 14 (2019) 1782–1793.

[91] Y. Wang, C. Shao, S. Qiu, Y. Zhu, M. Qin, Y. Meng, Y. Wang, H. Chu, Y. Zou, C. Xiang, J.-L. Zeng, Z. Cao, F. Xu, L. Sun, Nitrogen-doped porous carbon derived from ginkgo leaves with remarkable supercapacitance performance, Diamond and Related Materials. 98 (2019) 107475.